Progress In Electromagnetics Research B, Vol. 14, 449–477, 2009

THE UNIFIED THEORY OF NEAR-FIELD–FAR-FIELD TRANSFORMATIONS WITH SPIRAL SCANNINGS FOR NONSPHERICAL ANTENNAS

F. D'Agostino, F. Ferrara, C. Gennarelli, R. Guerriero and M. Migliozzi

Dipartimento di Ingegneria dell'Informazione ed Ingegneria Elettrica
University of Salerno
via Ponte Don Melillo, Fisciano (Salerno) 84084, Italy

Abstract—The unified theory of near-field–far-field transformations with spiral scannings for quasi-spherical antennas is extended in this paper to the case of nonspherical ones, i.e., antennas with two dimensions very different from the third one. To this end, these antennas are no longer considered as enclosed in a sphere, but in a proper convex domain bounded by a rotational surface. The extension, heuristically derived by paralleling the rigorous procedure valid for the spherical source modelling, allows one to overcome its main and serious drawbacks. In fact, the corresponding near-field–far-field transformations use a reduced number of near-field measurements and, above all, allow one to consider measurement surfaces at a distance smaller than one half the antenna maximum size, thus remarkably reducing the error related to the truncation of the scanning zone. These are very important features, which make the spiral scannings more and more appealing from the practical viewpoint. Some examples of the application of this theory to spirals wrapping the conventional scanning surfaces employed in the near-field–far-field transformations are reported, and the accuracy and robustness of the far-field reconstructions are assessed.

1. INTRODUCTION

Each member of the antenna measurement techniques community can profit today by about fifty years of research activity on near-field data acquisition and related near-field–far-field (NF–FF) transformation

Corresponding author: C. Gennarelli (gennar@diiie.unisa.it).

techniques [1–3]. In this framework, significant improvements in the performance of NF measurements have been recently achieved. They are based on the spatial bandlimitation properties of electromagnetic (EM) fields [4], on their nonredundant sampling representations [5], and on the optimal sampling interpolation (OSI) expansions of central type [6]. In particular, a significant reduction of the number of required NF data (and, as a consequence, of the measurement time) has been obtained for all the conventional scannings [7–12].

The use of the modulated scattering technique employing arrays of scattering probes, which allows a very fast electronic scanning, has been also proposed in [13] to reduce the time required for the acquisition of the NF data. However, antenna NF measurement facilities based on such a technique are not very flexible. A more viable way to reduce the time needed for the NF data acquisition is the employment of innovative spiral scanning techniques. They have been implemented, as suggested by Rahmat-Samii et al. in [14], by means of a continuous movement of the positioning systems of the probe and antenna under test (AUT). In particular, the helicoidal scanning [15], the planar [16] and spherical [17, 18] spiral scannings have been accomplished. In all the cases, by assuming the AUT enclosed in the smallest sphere able to contain it, a nonredundant sampling representation of the voltage data acquired by the measurement probe on the considered curve (helix or spiral) has been developed by applying the nonredundant representations of EM fields [5]. This, in addition to the choice of the curve step equal to the sample spacing needed to interpolate the data along the corresponding meridian curve (generatrix, radial line, meridian), has allowed one to get the desired two-dimensional OSI formula. It has been so possible to recover the NF data required by the NF–FF transformation technique using the corresponding conventional scanning [3]. Moreover, a unified theory of the spiral scannings has been provided in [19]. In fact, it has been proved that the voltage acquired by a nondirective probe can be reconstructed on a quite arbitrary rotational surface from a nonredundant number of its samples lying on a proper spiral wrapping the surface. The only required condition is that such a surface is obtained by rotating a meridian curve always external to the cone of vertex at the observation point and tangent to the sphere modelling the AUT. It is worth noting that the same interpolation scheme can be employed to recover the voltage, even if the spiral lies on geometrically different surfaces.

Unfortunately, the use of the spherical AUT modelling, even if quite general, prevents the possibility of considering measurement cylinders (planes) with a radius (distance) smaller than one half the

antenna maximum size. This drawback occurs in the helicoidal and in the planar spiral scannings when considering elongated and quasi-planar antennas, respectively, thus reflecting in an increase of the error related to the truncation of the scanning surface. In fact, for a given size of the scan zone, such an error raises on increasing the distance. Moreover, the "volumetrical" redundancy of the spherical modelling gives rise to an increase in the number of the NF data when the AUT geometry departs from the spherical one. When considering the spherical spiral scanning, the measurement region is not truncated, but the use of spherical AUT modelling reflects again in a useless growth of the needed measurements when dealing with elongated or quasi-planar antennas and, as a consequence, gives rise to an increase of the time required for the NF data acquisition.

A probe uncompensated NF–FF transformation technique with planar spiral scanning, which does not exhibit the previous constraint on the measurement plane distance, has been recently proposed in [20]. It uses the convolution property of the radiation integral and the fast Fourier transform (FFT) algorithm to efficiently evaluate the antenna far field directly from the acquired NF data. However, since such an approach, as that in [14], does not exploit the nonredundant representations of EM fields, it requires a useless large number of measurements. This comment holds also for the NF–FF transformation technique with helicoidal scanning [21].

The aim of this paper is to overcome the above drawbacks by properly extending the unified theory of the spiral scannings to the case of nonspherical antennas. To this end, an AUT with one or two predominant dimensions is no longer considered as enclosed in a sphere, but in a proper convex domain bounded by a rotational surface. Such an extension is derived, according to a heuristic reasoning, by paralleling the corresponding rigorous procedure valid when adopting the spherical AUT modelling. This new unified theory is then applied to spirals wrapping the conventional scanning surfaces employed in the NF–FF transformation techniques. To this end, effective source modellings, containing the spherical one as particular case, are adopted.

2. UNIFIED THEORY OF SPIRAL SCANNINGS FOR SPHERICAL AUTS

The main results concerning the unified theory of spiral scannings for antennas modelled as enclosed in a spherical surface [19] are summarized in this section.

Let us consider the field radiated by an AUT enclosed in a sphere

with radius a and observed on a regular curve C described by a proper parameterization $\underline{r} = \underline{r}(\xi)$. According to the theoretical results in [5], it is possible to consider the "reduced electric field"

$$\underline{F}(\xi) = \underline{E}(\xi)e^{j\gamma(\xi)} \tag{1}$$

where $\gamma(\xi)$ is a phase function to be determined. The bandlimitation error, occurring when $\underline{F}$ is approximated by a spatially bandlimited function, becomes negligible as the bandwidth exceeds a critical value W_ξ [5], so that it can be effectively controlled by choosing a bandwidth equal to $\chi' W_\xi$, χ' being an excess bandwidth factor slightly greater than unity for an electrically large AUT.

A nonredundant sampling representation of the EM field on the curve C can be obtained by using the following expressions for the phase function and parameterization [5]:

$$\gamma(s) = \frac{\beta}{2} \int_0^s \left[\max_{\underline{r'}} \hat{R} \cdot \hat{t} + \min_{\underline{r'}} \hat{R} \cdot \hat{t} \right] \mathrm{ds} \tag{2}$$

$$\xi = \xi(s) = \frac{\beta}{2W_\xi} \int_0^s \left[\max_{\underline{r'}} \hat{R} \cdot \hat{t} - \min_{\underline{r'}} \hat{R} \cdot \hat{t} \right] \mathrm{ds} \tag{3}$$

where $\underline{r'}$ denotes the source point, β is the wavenumber, s the curvilinear abscissa along C, $\hat{t}$ the unit vector tangent to it at the observation point P, and $\hat{R}$ the unit vector pointing from the source point to P. Hence, a change of W_ξ is reflected in a change of scale for ξ.

Let us suppose that the curve C is a spiral wrapping an arbitrary surface obtained by rotating a meridian curve always external to the cone having the vertex at P and tangent to the sphere enclosing the AUT. The coordinates of a point Q on such a spiral are given by:

$$\begin{cases} x = r(\theta)\sin\theta\cos\phi \\ y = r(\theta)\sin\theta\sin\phi \\ z = r(\theta)\cos\theta \end{cases} \tag{4}$$

where $r(\theta)$ is specified by the meridian curve generating the rotational surface, ϕ is the angular parameter describing the spiral and $\theta = k\phi$. For instance, when the surface is a plane at distance d (planar spiral) then $r(\theta) = d/\cos\theta$, if the surface is a cylinder of radius d (helix) then $r(\theta) = d/\sin\theta$, whereas $r(\theta) = d$ when a spiral wrapping a sphere of radius d is considered. It is worthy to note that the spiral angle θ, unlike the zenithal angle ϑ, can assume negative values. In

fact, when the spiral describes a complete round on the surface, θ varies in the range $[-\pi, \pi]$. Moreover, the spiral angle ϕ is always continuous, whereas, according to (4), the azimuthal angle φ exhibits a discontinuity jump of π when the spiral crosses the poles. Such a curve can be obtained by radially projecting on the observation surface a proper spiral wrapping the AUT sphere.

In order to allow the two-dimensional interpolation, the angular step of the spiral must be equal to the sample spacing needed to interpolate the field along the meridian curve. Therefore, the parameter k is chosen such that the spiral step, determined by two consecutive intersections (at ϕ and $\phi+2\pi$) with the considered meridian curve, is equal to $\Delta\theta = \Delta\vartheta = 2\pi/(2N'' + 1)$, with $N'' = \mathrm{Int}(\chi N') + 1$ and $N' = \mathrm{Int}(\chi'\beta a) + 1$, $\mathrm{Int}(x)$ denoting the integer part of x and $\chi > 1$ being an oversampling factor which allows one to control the truncation error. Since $\Delta\theta = 2\pi k$, it results $k = 1/(2N'' + 1)$.

It can be convenient to impose the passage of the spiral through a given point P_0 of the meridian curve at $\varphi = 0$. As a consequence, the coordinates of Q become:

$$\begin{cases} x = r(\theta)\sin\theta\cos(\phi - \phi_i) \\ y = r(\theta)\sin\theta\sin(\phi - \phi_i) \\ z = r(\theta)\cos\theta \end{cases} \tag{5}$$

ϕ_i being the value of ϕ at P_0.

It can be verified that the extreme values of $\hat{R} \cdot \hat{t}$ are determined by considering the intersection of the plane defined by $\hat{t}$ and the unit

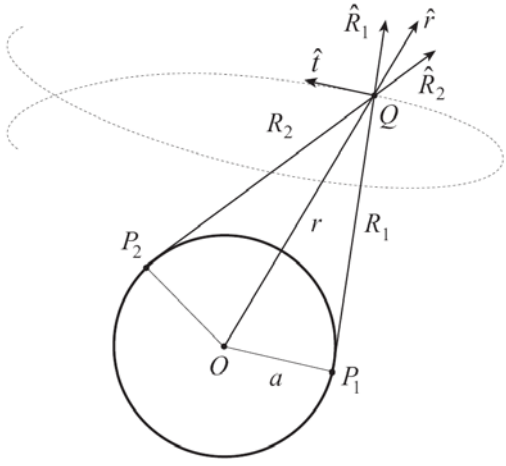

Figure 1. Geometry of the problem in the plane $\hat{t}$, $\hat{r}$.

vector $\hat{r}$ (pointing from the origin to Q) with the cone having the vertex at Q and the generatrices coincident with the tangents to the sphere enclosing the AUT (see Fig. 1). By simple geometrical considerations and after some analytical manipulations, it results [19]:

$$\gamma = \beta \int_0^r \sqrt{1 - a^2/r'^2} dr' = \beta\sqrt{r^2 - a^2} - \beta a \cos^{-1}\left(\frac{a}{r}\right) \tag{6}$$

$$\xi = \frac{\beta a}{W_\xi} \int_0^\phi \sqrt{k^2 + \sin^2 k\phi'} d\phi' \tag{7}$$

Note that, when adopting a spherical AUT modelling, the expression (6) of the phase function relevant to the sampling representation along the spiral coincides with that relevant to the representation on a meridian curve [5]. Moreover, according to (7), ξ is β/W_ξ times the arclength along the spiral wrapping the sphere modelling the source. Since such a spiral is a closed curve, it is convenient to choose the bandwidth W_ξ such that the parameter ξ covers a 2π range when the whole projecting curve is described. Therefore,

$$W_\xi = \frac{\beta a}{\pi} \int_0^{(2N''+1)\pi} \sqrt{k^2 + \sin^2 k\phi'} d\phi' \tag{8}$$

By taking into account the above representation, the OSI formula for reconstructing the reduced field at any point Q of the spiral is [5, 19]:

$$\underline{F}(\xi) = \sum_{m=m_0-p+1}^{m_0+p} \underline{F}(\xi_m) \Omega_M(\xi - \xi_m) D_{M''}(\xi - \xi_m) \tag{9}$$

where $m_0 = \mathrm{Int}[(\xi - \xi(\phi_i))/\Delta\xi]$ is the index of the sample nearest (on the left) to the point Q, $2p$ the number of retained samples $\underline{F}(\xi_m)$, and

$$\xi_m = \xi(\phi_i) + m\Delta\xi = \xi(\phi_i) + 2\pi m/(2M'' + 1) \tag{10}$$

with $M'' = \mathrm{Int}(\chi M') + 1$ and $M' = \mathrm{Int}(\chi' W_\xi) + 1$. Moreover,

$$\begin{aligned} D_{M''}(\xi) &= \frac{\sin((2M''+1)\xi/2)}{(2M''+1)\sin(\xi/2)}; \\ \Omega_M(\xi) &= \frac{T_M[-1 + 2(\cos(\xi/2)/\cos(\overline{\xi}/2))^2]}{T_M[-1 + 2/\cos^2(\overline{\xi}/2)]} \end{aligned} \tag{11}$$

are the Dirichlet and Tschebyscheff Sampling functions, wherein $T_M(\xi)$ is the Tschebyscheff polynomial of degree $M = M'' - M'$ and $\overline{\xi} = p\Delta\xi$.

It must be stressed that, when interpolating the field in the neighbourhood of the poles ($\vartheta = 0$ and $\vartheta = \pi$), the excess bandwidth factor χ' must be properly increased to avoid a significant growth of the bandlimitation error. This is due to the fact that small variations of ξ correspond to very large changes of ϕ in these zones.

The OSI formula (9) can be used to evaluate the "intermediate samples", namely, the reduced field values at the intersection points between the spiral and the meridian curve passing through the observation point P. Once these samples have been evaluated, the reduced field at P can be reconstructed via the following OSI expansion:

$$\underline{F}(\vartheta, \varphi) = \sum_{n=n_0-q+1}^{n_0+q} \underline{F}(\vartheta_n)\Omega_N(\vartheta - \vartheta_n)D_{N''}(\vartheta - \vartheta_n) \tag{12}$$

where $N = N'' - N'$, $n_0 = \mathrm{Int}[(\vartheta - \vartheta_0)/\Delta\vartheta]$, $2q$ is the number of the retained intermediate samples $\underline{F}(\vartheta_n)$, and

$$\vartheta_n = \vartheta_n(\varphi) = \vartheta(\phi_i) + k\varphi + n\Delta\vartheta = \vartheta_0 + n\Delta\vartheta \tag{13}$$

3. THE UNIFIED THEORY OF SPIRAL SCANNINGS FOR NONSPHERICAL ANTENNAS

The goal of this section is just the extension of the previous sampling representation to the case of nonspherical antennas, i.e., those having one or two predominant dimensions. When dealing with these antennas, it is no longer convenient to adopt the smallest sphere as surface enclosing them but, as suggested in [5], a proper rotational surface Σ bounding a convex domain. According to a heuristic reasoning, such an extension is derived by paralleling the corresponding rigorous procedure valid for the spherical AUT modelling. It is so possible to get a sampling representation, which allows one to reconstruct the field at any point on a quite arbitrary rotational surface from a nonredundant number of its samples lying on a proper spiral wrapping the surface. The only requirement is that the surface is obtained by rotating a meridian curve always external to the cone of vertex at the observation point P and tangent to the surface Σ modelling the AUT.

The parameterization η and the corresponding phase function ψ to be used for obtaining a nonredundant sampling representation along a meridian curve can be derived by taking into account that the extreme values of the inner product $\hat{R} \cdot \hat{t}$ in (2) and (3) occur (see Fig. 2) at

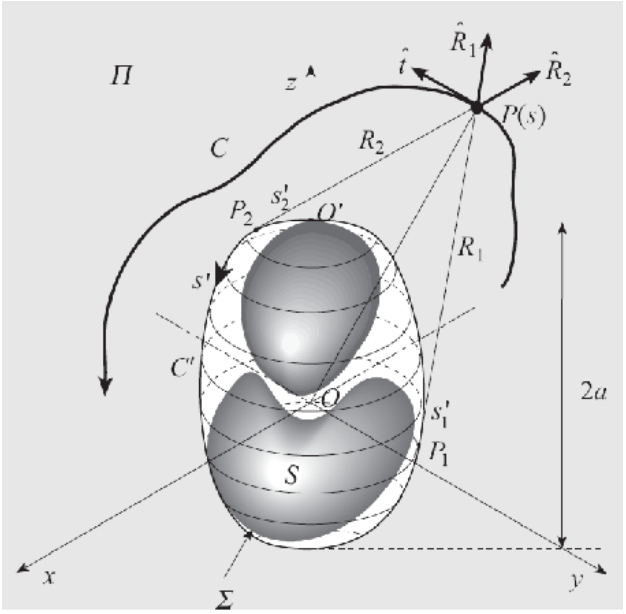

Figure 2. Relevant to a meridian observation curve.

the two tangency points $P_{1,2}$ on C' (intersection curve between the meridian plane Π and Σ). Accordingly, by choosing

$$W_\eta = \beta \ell'/2\pi \tag{14}$$

ℓ' being the length of C', it results [5]:

$$\eta = \frac{\pi}{\ell'}[R_1 - R_2 + s_1' + s_2'] \tag{15}$$

$$\psi = \frac{\beta}{2}[R_1 + R_2 + s_1' - s_2'] \tag{16}$$

where $s_{1,2}'$ are the arclength coordinates of $P_{1,2}$ and $R_{1,2}$ the distances from P to $P_{1,2}$.

Some intriguing questions now arise. What are the equations of the spiral, the parameter ξ for describing it, and the phase factor γ to be multiplied by the field expression when interpolating along it?

By paralleling the procedure of the previous section, the spiral can be obtained by projecting on the observation surface a proper spiral that wraps around the surface Σ modelling the AUT. The step of such a spiral is equal to the sample spacing $\Delta\eta = 2\pi/(2N'' + 1)$ needed to interpolate the field along a meridian curve. Note that, as before,

$N'' = \mathrm{Int}(\chi N') + 1$, but now $N' = \mathrm{Int}(\chi' W_\eta) + 1$. The projection is obtained by the curves at $\eta = \mathrm{const}$ that, in such a case, take the role of the radial lines of the spherical modelling. Accordingly, the parametric Equations (5) of the spiral become:

$$\begin{cases} x = r[\theta(\eta)] \sin\theta(\eta) \cos(\phi - \phi_i) \\ y = r[\theta(\eta)] \sin\theta(\eta) \sin(\phi - \phi_i) \\ z = r[\theta(\eta)] \cos\theta(\eta) \end{cases} \tag{17}$$

wherein $\eta = k\phi = \phi/(2N'' + 1)$.

Again, a heuristic reasoning allows the determination of the parameterization ξ and phase factor γ to be used for obtaining a nonredundant sampling representation along the spiral. In particular, by generalizing the corresponding relations for the case of spherical modelling (see (6) and (7)), γ coincides with the phase function ψ relevant to a meridian curve, and ξ is β/W_ξ times the arclength of the projecting point that lies on the spiral wrapping the surface Σ. Moreover, W_ξ is chosen equal to β/π times the length of the spiral wrapping Σ from pole to pole. Namely, the spiral, γ and ξ are such that they coincide with those relevant to the spherical modelling when the surface Σ leads to a sphere.

The OSI expansion (9) can be still employed to recover the intermediate samples. Once these samples have been evaluated, the field at any point P on the observation surface can be reconstructed via the following OSI expansion:

$$\underline{F}(\eta(\vartheta), \varphi) = \sum_{n=n_0-q+1}^{n_0+q} \underline{F}(\eta_n) \Omega_N(\eta - \eta_n) D_{N''}(\eta - \eta_n) \tag{18}$$

where $N = N'' - N'$, $n_0 = \mathrm{Int}[(\eta - \eta_0)/\Delta\eta]$, $2q$ is the number of the retained intermediate samples $\underline{F}(\eta_n)$, and

$$\eta_n = \eta_n(\varphi) = \eta_n(\phi_i) + k\varphi + n\Delta\eta = \eta_0 + n\Delta\eta \tag{19}$$

Since the voltage measured by a nondirective probe has the same effective spatial bandwidth of the field [22], the previous OSI expansions can be used also to interpolate the "reduced voltage" $\tilde{V}(\xi) = V(\xi) e^{\mathrm{j}\gamma(\xi)}$.

It must be stressed that these results can be directly applied to spirals wrapping the scanning surfaces usually employed in the classical NF–FF transformations [3].

Let us now discuss the reasons for using a heuristic approach. First of all, the rigorous analytical determination of the optimal spiral and the evaluation of the corresponding phase factor and parameterization

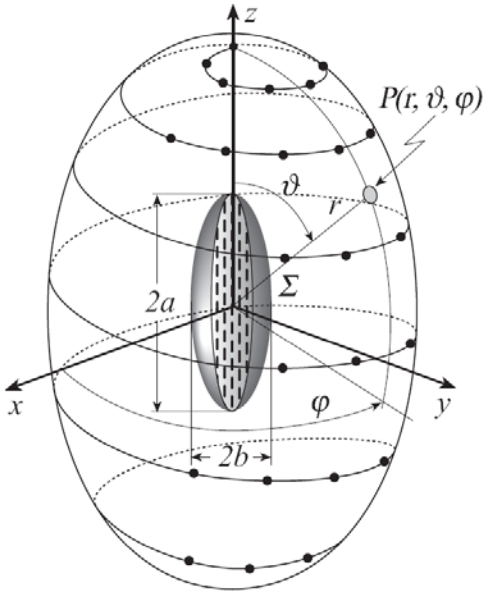

Figure 3. Ellipsoidal spiral scanning.

become much more difficult or impossible, since some analytical considerations are no longer valid when adopting a modelling different from the spherical one. On the other hand, the heuristic approach gives an easy to handle tool to determine them for different AUT modellings, as will be shown in the following sections.

4. THE ELLIPSOIDAL SPIRAL CASE

The results derived in the previous section are here applied to the particular case of an elongated antenna and a spiral lying on a prolate ellipsoid. It is worthy to note that, although the considered case has been tackled for its generality, the related OSI algorithm allows one to recover the NF data required by the NF–FF transformation process [23].

An effective modelling for an elongated antenna is obtained by considering it as enclosed in the smallest prolate ellipsoid having major and minor semi-axes equal to a and b (see Fig. 3). In such a case, the bandwidth W_η, the optimal expressions for the phase factor ψ and parameterization η relevant to a meridian curve become [5]:

$$W_\eta = \frac{4a}{\lambda}\mathrm{E}(\pi/2|\varepsilon^2) \tag{20}$$

$$\psi = \beta a\left[v\sqrt{\frac{v^2-1}{v^2-\varepsilon^2}} - \mathrm{E}\left(\cos^{-1}\sqrt{\frac{1-\varepsilon^2}{v^2-\varepsilon^2}}|\varepsilon^2\right)\right] \tag{21}$$

$$\eta = \frac{\pi}{2}\left[1+\frac{\mathrm{E}(\sin^{-1}u|\varepsilon^2)}{\mathrm{E}(\pi/2|\varepsilon^2)}\right] \tag{22}$$

where λ is the wavelength, $u=(r_1-r_2)/2f$ and $v=(r_1+r_2)/2a$ are the elliptic coordinates, $r_{1,2}$ being the distances from P to the foci and $2f$ the focal distance of C'. Moreover, $\varepsilon = f/a$ is the eccentricity of C' and $\mathrm{E}(\cdot|\cdot)$ denotes the elliptic integral of second kind. It is worth noting that in any meridian plane the curves $\psi=$ const and $\eta=$ const are ellipses and hyperbolas confocal to C'.

The spiral wraps a prolate ellipsoid (Fig. 3) having major and minor semi-axes equal to a_e and b_e. Such an ellipsoid can be described by the parametric equations

$$\begin{cases} x = b_e\cos\alpha\cos\varphi \\ y = b_e\cos\alpha\sin\varphi \\ z = \alpha_e\sin\alpha \end{cases} \tag{23}$$

where the angular-like parameter $\alpha = \tan^{-1}(b_e/(a_e\tan\vartheta))$ varies in the range $[-\pi/2,\pi/2]$. Therefore, the coordinates of a point on the spiral are given by:

$$\begin{cases} x = b_e\cos\delta\cos\phi \\ y = b_e\cos\delta\sin\phi \\ z = a_e\sin\delta \end{cases} \tag{24}$$

where, due to the aforementioned behaviour of the spiral around the poles,

$$\delta = \delta(\eta) = \tan^{-1}\left[\frac{b_e}{a_e\tan\theta(\eta)}\right] + i\pi \tag{25}$$

with

$$i = \begin{cases} +1 & -\pi/2 < \theta(\eta) < 0 \\ 0 & \theta(\eta) > 0 \\ -1 & -\pi < \theta(\eta) < -\pi/2 \end{cases} \tag{26}$$

Accordingly, the angular-like parameter δ covers the range $[-\pi,\pi]$ when the spiral describes a complete round on the surface.

It can be verified that, in the ellipsoidal spiral case, it results

$$r[\theta(\eta)] = \sqrt{b_e^2\cos^2\delta + a_e^2\sin^2\delta} \tag{27}$$

and the unit vector tangent to the meridian curve is given by:

$$\hat{\tau} = \frac{-b_e \sin\alpha(\hat{x}\cos\varphi + \hat{y}\sin\varphi) + \hat{z}a_e\cos\alpha}{\sqrt{b_e^2\sin^2\alpha + a_e^2\cos^2\alpha}} \tag{28}$$

Some numerical tests assessing the effectiveness of the developed sampling representation are reported. They refer to a uniform planar array (Fig. 3) of elementary Huygens sources polarized along the z axis and spaced of 0.5λ. Its elements cover an elliptical zone in the plane $y = 0$, with major and minor semi-axes equal to 30λ and 10λ, respectively. The scanning spiral lies on a prolate ellipsoid with $a_e = 45\lambda$ and $b_e = 25\lambda$.

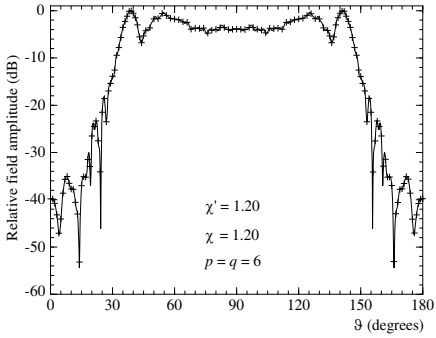

Figure 4. Amplitude of the field τ-component on the meridian curve at $\varphi = 90°$. Solid line: exact. Crosses: interpolated.

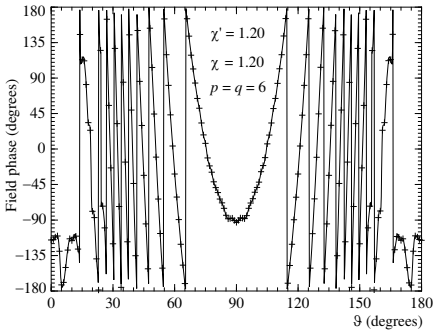

Figure 5. Phase of the field τ-component on the meridian curve at $\varphi = 90°$. Solid line: exact. Crosses: interpolated.

Figures 4 and 5 show the reconstruction of the amplitude and phase of the electric field τ-component (the most significant one) on the meridian curve at $\varphi = 90°$. As can be seen, there is an excellent agreement between the exact field and the reconstructed one. It is useful to note that, in order to avoid a significant growth of the bandlimitation error, an excess bandwidth factor such that the sample spacing is reduced exactly by a factor 9 has been adopted in the zones of the spiral determined by the 80 samples around the poles.

The accuracy in the NF interpolation process is also confirmed by the values of the maximum and mean-square reconstruction errors (normalized to the field maximum value on the ellipsoid) reported in Figs. 6 and 7, for $p = q$ ranging from 3 to 10, $\chi' = 1.20$ (save for the polar zones) and $\chi = 1.10, 1.15, 1.20, 1.25$. As expected, they decrease up to very low values on increasing the oversampling factor and/or the retained samples number.

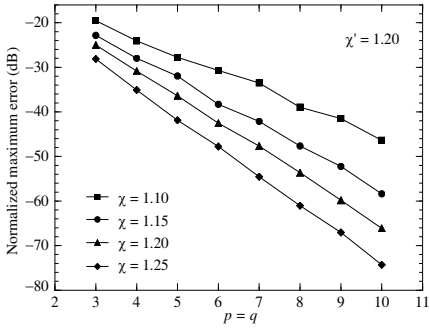

Figure 6. Maximum reconstruction error of the field τ-component.

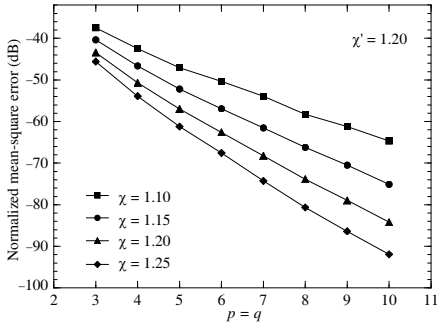

Figure 7. Mean-square reconstruction error of the field τ-component.

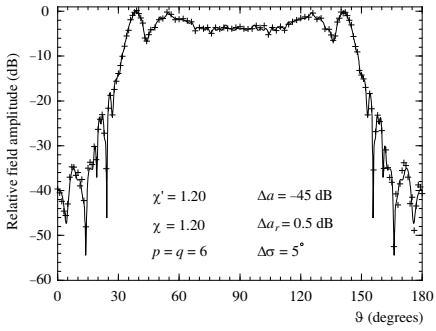

Figure 8. Amplitude of the field τ-component on the meridian curve at $\varphi = 90°$. Solid line: exact. Crosses: reconstructed from error affected data.

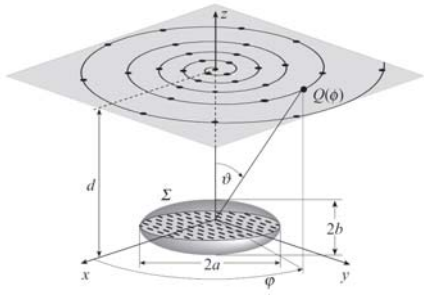

Figure 9. Planar spiral scanning: oblate ellipsoidal AUT modelling.

The algorithm stability has been investigated by adding random errors to the exact data. These errors simulate a background noise (bounded to Δa in amplitude and with arbitrary phase) and an uncertainty on the field samples of $\pm\Delta a_r$ in amplitude and $\pm\Delta\sigma$ in phase. As shown in Fig. 8, the interpolation algorithm is stable.

It is useful to note that the number of samples over the spiral is 25 270. In particular, the number of "regular samples" at spacing $\Delta\xi$ is 23 990, whereas the number of "extra samples" at reduced spacing is 1 280.

5. NF–FF TRANSFORMATION WITH PLANAR SPIRAL SCANNING

The planar spiral scanning, as all the planar ones, is particularly suitable for highly directive antennas which radiate pencil beam patterns well within the solid angle specified by the edges of the AUT and those of the scanning area. Usually, these antennas exhibit a quasi-planar geometry so that the spherical AUT modelling adopted in [16, 19] gives rise to an useless increase in the number of NF data and prevents the possibility of considering measurement planes at distances less than half of the AUT maximum dimension, thus increasing the error related to the truncation of the scanning zone.

These drawbacks can be overcome by adopting an oblate ellipsoidal AUT modelling, already employed in the plane-polar scanning case [9]. Accordingly, by considering the AUT as enclosed in the smallest oblate ellipsoid with major and minor semi-axes equal to a and b (see Fig. 9), the bandwidth W_η and the phase factor ψ relevant to a radial line are given by (20) and (21), respectively, whereas the parameterization η becomes [5, 24]:

$$\eta = \frac{\pi}{2} \frac{\mathrm{E}(\sin^{-1} u|\varepsilon^2)}{\mathrm{E}(\pi/2|\varepsilon^2)} \tag{29}$$

According to the unified theory of spiral scans described in Section 3, the planar spiral is obtained by projecting the spiral wrapping the oblate ellipsoid modelling the AUT on the scanning plane via the hyperbolas at $\eta = \text{const}$ [24]. By taking into account that $r[\theta(\eta)] = d/\cos\theta(\eta)$ and $\phi_i = 0$ for a planar spiral, the parametric Equations (17) become:

$$\begin{cases} x = d\tan\theta(\eta)\cos\phi = \rho(\eta)\cos\phi \\ y = d\tan\theta(\eta)\sin\phi = \rho(\eta)\sin\phi \\ z = d \end{cases} \tag{30}$$

The aforementioned drawbacks can be also overcome by adopting the "flexible" source modelling already successfully employed with reference to the plane-polar scanning [8]. The surface Σ is now formed by two circular "bowls" with the same aperture diameter $2a$ (see Fig. 10). It is useful to note that their lateral surfaces have not the same bend because they are generally determined by rotating two different circular arcs, each equal to a quarter of circumference (with radius c and c'). Such a kind of surface allows one to fit very well a lot of real antennas by properly setting the parameters, namely c, c' and a. For instance, Σ coincides with a spherical surface if $c = c' = a$, it becomes

a half-sphere if $c = 0$ and $c' = a$, and it reduces to a circular dish for $c = c' = 0$. According to the results in Section 3, the bandwidth W_η, the expressions for the phase factor ψ and parameterization η relevant to a radial line are given by relations (14)–(16). In such a case [8],

$$\ell' = 2[(a - c) + (a - c') + (c + c')\pi/2] \tag{31}$$

whereas the expressions of the distances $R_{1,2}$ from the observation point P to the tangency points $P_{1,2}$ on C', and of their arclength coordinates $s'_{1,2}$ change depending on the location of $P_{1,2}$. In particular, when they are both located on the upper bowl ($\rho < a$), it results [8]:

$$R_1 = \sqrt{(\rho + b)^2 + d^2 - c^2}; \qquad s'_1 = -(b + c\alpha_1) \tag{32}$$

$$\alpha_1 = \tan^{-1}(R_1/c) - \tan^{-1}[(\rho + b)/d]; \qquad b = a - c \tag{33}$$

$$R_2 = \sqrt{(b - \rho)^2 + d^2 - c^2}; \qquad s'_2 = b + c\alpha_2 \tag{34}$$

$$\alpha_2 = \tan^{-1}(R_2/c) - \tan^{-1}[(b - \rho)/d] \tag{35}$$

When P_2 is on the lower bowl ($\rho \geq a$), the expressions of R_1, s'_1 and α_1 are again given by relations (32) and (33), whereas it results:

$$R_2 = \sqrt{(\rho - b')^2 + d^2 - c'^2}; \qquad s'_2 = b + c\pi/2 + c'\alpha_2 \tag{36}$$

$$\alpha_2 = \tan^{-1}(R_2/c') - \pi/2 + \tan^{-1}[(\rho - b')/d]; \quad b' = a - c' \tag{37}$$

The parametric equations of the spiral are formally the same of the ellipsoidal modelling case, but obviously the projecting curves at $\eta = \text{const}$ are no more hyperbolas.

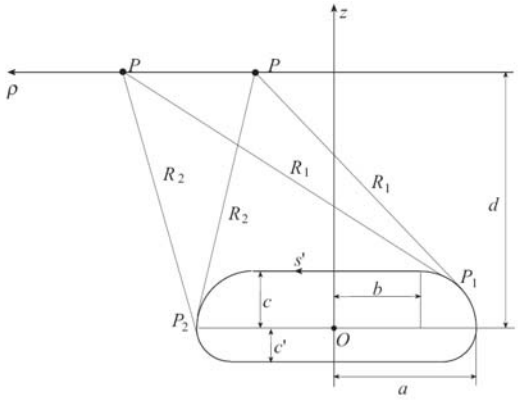

Figure 10. Geometry of the flexible source modelling.

Only some results relevant to the use of the flexible source modelling are shown. The interested reader can refer to [24] for application examples relevant to the ellipsoidal modelling case. It is worth noting that an example, highlighting the advantage from the truncation error viewpoint in using the ellipsoidal AUT modelling instead of spherical one, can be also found in this last paper. The simulations reported in the following are relevant to four uniform planar circular arrays placed at $z = -4\lambda, -1\lambda, 2\lambda, 5\lambda$ and fitted by the described source modelling with $a = 18\lambda$, $c = 5\lambda$, and $c' = 4\lambda$. Their elements are elementary Huygens sources linearly polarized along y and spaced of 0.7λ along the radial and azimuthal lines. An open-ended circular waveguide with radius $a' = 0.338\lambda$ is chosen as probe in order to avoid the probe co-rotation. In fact, when using probes exhibiting only a first-order azimuthal dependence in their radiated far field (as an open-ended cylindrical waveguide excited by a TE_{11} mode), there is no need of co-rotation, since V_V and V_H can be evaluated from the measured voltages V_φ and V_ρ via the relations [16]:

$$V_V = V_\varphi \cos\varphi - V_\rho \sin\varphi; \; V_H = V_\varphi \sin\varphi + V_\rho \cos\varphi \qquad (38)$$

The scanning plane distance d is 10λ and the NF samples have been acquired on a spiral covering a circular zone of radius 57λ (apart from the guard samples).

Figure 11 shows a representative reconstruction example of the amplitude of the voltage V_V on the radial line at $\varphi = 90°$. As it can be seen, the recovery is everywhere very accurate. In the reported example, the sample spacing has been reduced by a factor

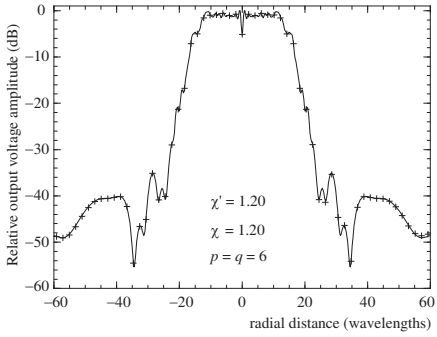

Figure 11. Amplitude of V_V on the radial line at $\varphi = 90°$. Solid line: exact. Crosses: interpolated.

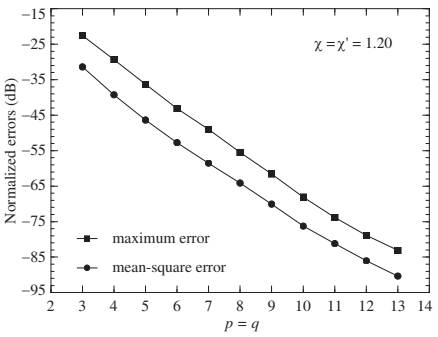

Figure 12. Normalized maximum and mean-square reconstruction errors of V_V.

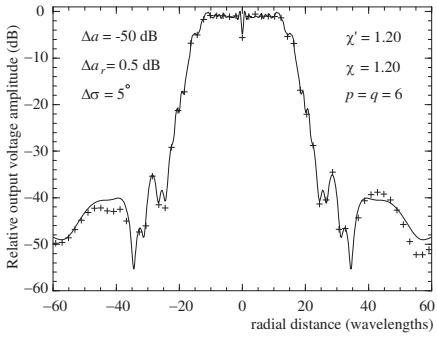

Figure 13. Amplitude of V_V on the radial line at $\varphi = 90°$. Solid line: exact. Crosses: interpolated from error affected data.

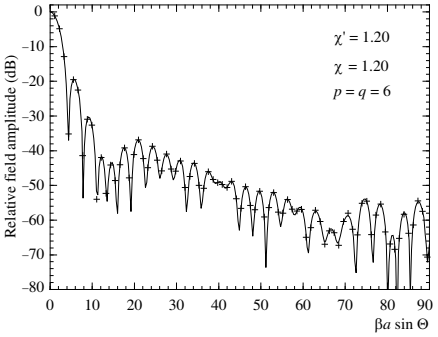

Figure 14. FF pattern in the E-plane. Solid line: exact field. Crosses: reconstructed from NF data acquired via planar spiral scanning.

5 in the zone of the spiral determined by the 21 samples centered on the pole, in order to avoid a significant growth of the bandlimitation error when interpolating nearby the pole. The algorithm performances are confirmed by the attained values of the normalized maximum and mean-square reconstruction errors, reported in Fig. 12 for $\chi = \chi' = 1.20$ and $p = q$ ranging from 3 to 13. The voltage reconstruction displayed in Fig. 13, which refers to the same radial line of Fig. 11 but obtained from error affected data, assesses the robustness of the developed algorithm.

The described sampling representation has been applied also for recovering the plane-rectangular data lying in a $80\lambda \times 80\lambda$ square grid needed by the classical NF–FF transformation [25]. The corresponding E-plane pattern is shown in Fig. 14. As can be seen, the FF reconstruction is very accurate also in the far out side lobes region (characterized by very low field levels), thus confirming the effectiveness of the technique.

Note that the samples number on the spiral is 11 152, remarkably less than that needed by the NF–FF transformation [25]. In particular, the number of "regular" samples at spacing $\Delta\xi$ is 11 072, whereas the number of "extra samples" at reduced spacing is 80.

6. NF–FF TRANSFORMATION WITH HELICOIDAL SCANNING

The helicoidal scanning, as the cylindrical one, allows the reconstruction of the antenna complete radiation pattern save for the zones surrounding the spherical polar angles. Accordingly, it is particularly attractive when considering antennas that concentrate the EM radiation in an angular region centred on the horizontal plane, as the radiating systems for radio base stations. Usually, these antennas are elongated, i.e., have a predominant dimension. Accordingly, the use of a sphere to model them, as in [15, 19], does not permit to consider measurement cylinders with radius d less than one half the AUT maximum size, thus increasing the truncation error. In addition, the redundancy of the spherical modelling reflects in a useless growth of the NF data number for these antennas.

To overcome these drawbacks, two efficient probe compensated NF–FF transformation techniques with helicoidal scanning, which make use of effective source modellings tailored for elongated antennas, are described in this section. The former [26] makes use of a prolate ellipsoidal model of the AUT (see Fig. 15), whereas the latter [27] employs a very effective modelling wherein the surface Σ enclosing the AUT is a cylinder ended in two half-spheres (Fig. 16), referred in the following as the rounded cylindrical modelling.

When the AUT is considered as enclosed in the smallest prolate ellipsoid with major and minor semi-axes equal to a and b, the bandwidth W_η, the phase factor ψ and the parameterization η relevant to a generatrix are explicitly [11, 26] given by (20)–(22). Whereas, when adopting the rounded cylindrical modelling, their expressions can be obtained by the general ones (14)–(16) by properly taking into account the geometry of the surface Σ (Fig. 16). By lengthy, but straightforward computations, it can be easily verified that, in such a case [10, 27],

$$\ell' = 2(h' + \pi a'); \qquad R_{1,2} = \sqrt{(z \mp h'/2)^2 + d^2 - a'^2} \tag{39}$$

$$s'_1 = a' \sin^{-1}\left(\frac{a'd + R_1((h'/2) - z)}{R_1^2 + a'^2}\right) \tag{40}$$

$$s'_2 = h' + a'\left[\pi - \sin^{-1}\left(\frac{a'd + R_2((h'/2) + z)}{R_2^2 + a'^2}\right)\right] \tag{41}$$

wherein h' and a' are the geometrical parameters specifying the rounded cylinder, i.e., the height of the cylinder and the radius of the two half-spheres.

The scanning helix, the optimal parameter for describing it, and

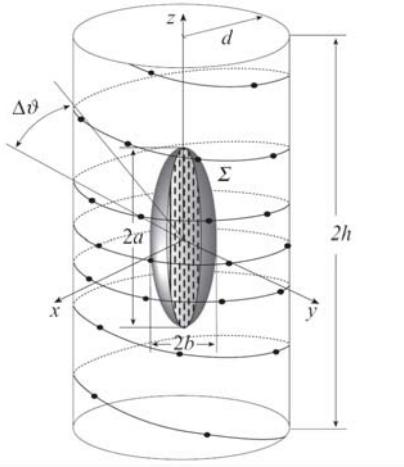

Figure 15. Helicoidal scanning: prolate ellipsoidal AUT modelling.

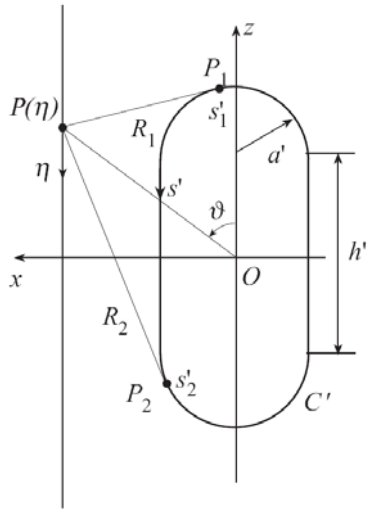

Figure 16. Relevant to the rounded cylindrical modelling.

the optimal phase factor to be extracted from the voltage expression when interpolating along it can be determined according to the unified theory described in Section 3. In particular, the helix is obtained by projecting the spiral wrapping the surface Σ modelling the AUT on the cylinder via the curve at $\eta = \text{const}$, that, obviously, are hyperbolas in the prolate ellipsoidal case. In both the cases, by taking into account that $r[\theta(\eta)] = d/\sin\theta(\eta)$ for a helix, the parametric Equations (17) become:

$$\begin{cases} x = d\cos(\phi - \phi_i) \\ y = d\sin(\phi - \phi_i) \\ z = d\cot[\theta(\eta)] \end{cases} \tag{42}$$

The following results are relevant to the use of the rounded cylinder modelling, whereas, those assessing the effectiveness of the prolate ellipsoidal one can be found in [26]. They are relevant to a uniform planar array of 0.6λ spaced elementary Huygens sources, polarized along the z axis and covering a zone in the plane $y = 0$, formed by a rectangle ended in two half-circles. The sizes of the rectangle are: $2a' = 12\lambda$ and $h' = 45\lambda$. The helix wraps a cylinder with radius $d = 12\lambda$ and height $2h = 140\lambda$. An open-ended WR-90 rectangular waveguide, operating at the frequency of 10 GHz, is considered as probe. A representative reconstruction example of the

amplitude of the output voltage V on the generatrix at $\varphi = 90°$ is shown in Fig. 17. As can be seen, the reconstruction is everywhere very accurate. The values of the maximum and mean-square errors (normalized to the voltage maximum value on the cylinder), reported in Fig. 18 for $\chi = \chi' = 1.20$ and $p = q$ ranging from 3 to 14, confirm the accuracy of the sampling representation.

The described interpolation algorithm has been applied to recover the NF data needed to perform the classical NF–FF transformation [28]. The corresponding E-plane pattern is shown in

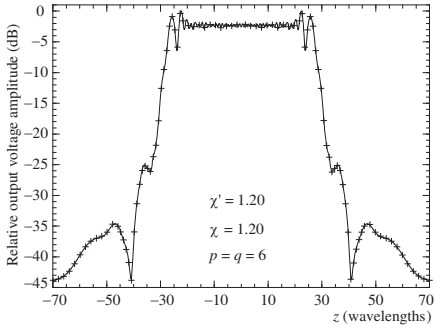

Figure 17. Amplitude of V on the generatrix at $\varphi = 90°$. Solid line: exact. Crosses: interpolated.

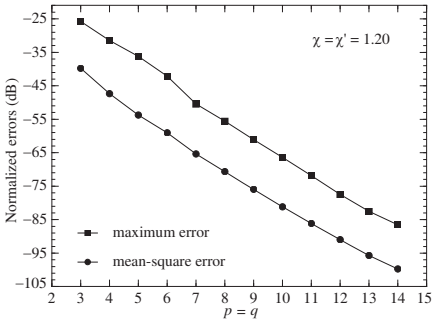

Figure 18. Normalized maximum and mean-square reconstruction errors of V.

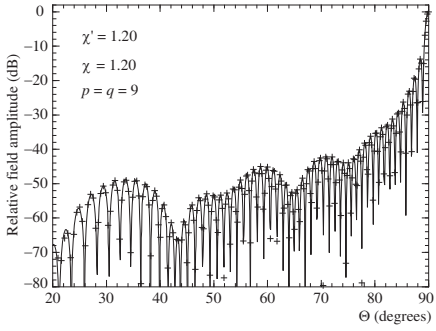

Figure 19. E-plane pattern. Solid line: exact. Crosses: reconstructed from NF data acquired via the helicoidal scanning.

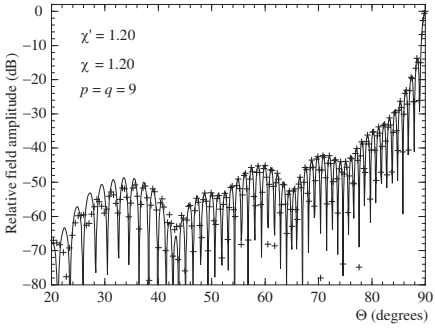

Figure 20. E-plane pattern. Solid line: exact. Crosses: reconstructed from NF data acquired via the helicoidal scanning when using the spherical modelling.

Fig. 19. As can be seen, the exact and recovered fields are practically indistinguishable. Note that the number of employed samples (guard samples included) for reconstructing the NF data on the considered cylinder is 17 884, about one half than that (35 968) required by the approach in [21], and comparable with that (19 357) needed by the nonredundant NF–FF transformation with cylindrical scanning [10].

As already stated, the use of the spherical AUT modelling prevents the possibility of considering scanning cylinders with a radius smaller than one half the antenna maximum dimension and this reflects in an increase of the truncation error for a given size of the measurement zone. In order to point out this shortcoming, another reconstruction of the E-plane pattern obtained by adopting the spherical modelling is shown in Fig. 20. In such a case, the NF data have been acquired on a helix that covers a cylinder having the same height but radius of 30λ. As can be clearly seen, the reconstruction is less accurate in the far out side lobe region.

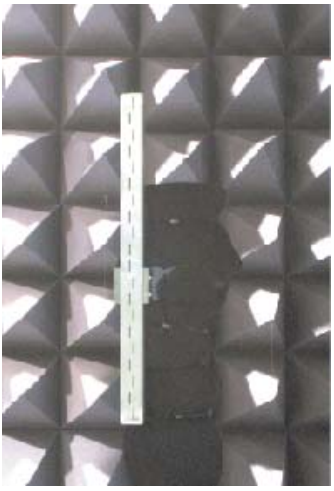

Figure 21. Photo of the slotted antenna.

At last, an experimental validation of the NF–FF transformation technique using the ellipsoidal AUT modelling is provided [29]. It has been carried out in the anechoic chamber available at the laboratory of antenna characterization of the University of Salerno, which is provided with a cylindrical NF facility system supplied by MI Technologies. The probe is an open-ended rectangular waveguide MI-6970-WR90, whose end is tapered for minimizing the diffraction effects. The AUT, located in the plane $x = 0$, is a resonant slotted waveguide array 37.7 cm long (see Fig. 21), fed at the center of the bottom broad wall by a

coaxial line, operating at 10 GHz. It has been obtained from a WR-90 waveguide by cutting in it two rows each of 10 round-ended slots. These rows are at the same distance from the center line of the broad waveguide wall. The slots are longitudinally directed and uniformly spaced by $\lambda_g/2$, wherein λ_g is the guide wavelength. According to the described sampling representation, the AUT has been modelled as enclosed in a prolate ellipsoid with major and minor semi-axes equal to 21 cm and 4.2 cm. The probe voltages have been collected on a helix lying on a cylinder having $d = 18$ cm and $2h = 230.85$ cm. The FF pattern in the principal planes H and E, reconstructed from the acquired helicoidal NF data, is compared in Figs. 22 and 23 with that obtained by using the software package MI-3000 from the knowledge of the data directly measured on the classical cylindrical grid. The same software has been used to get the FF reconstructions from the helicoidal NF data. To this end, the two-dimensional OSI algorithm (with $\chi' = 1.35$, $\chi = 1.20$, and $p = q = 6$) has been employed for recovering the cylindrical data required to carry out the NF–FF transformation. As can be seen, in both the planes, there is a very good agreement, thus assessing the validity of such a NF–FF transformation with helicoidal scanning.

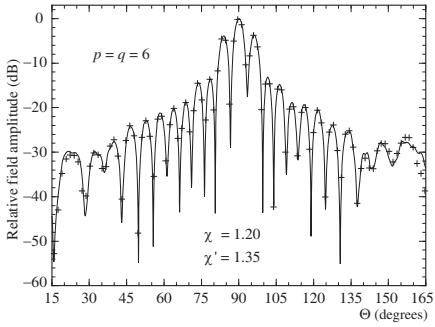

Figure 22. H-plane pattern. Solid line: reference. Crosses: reconstructed from NF measurements acquired via helicoidal scanning.

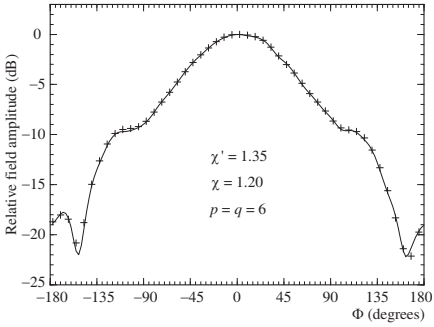

Figure 23. E-plane pattern. Solid line: reference. Crosses: reconstructed from NF measurements acquired via helicoidal scanning.

7. NF–FF TRANSFORMATION WITH SPHERICAL SPIRAL SCANNING

The NF–FF transformation technique with spherical spiral scanning, as that employing the classical spherical scanning, gives the full antenna pattern coverage, even though the data processing is considerably more complicated than that needed by the NF–FF transformation techniques using planar and cylindrical NF facilities.

In a spherical NF measurement facility, the scanning region is not truncated, but the use of spherical AUT modelling reflects again in a useless growth of the needed measurements when the AUT geometry departs from the spherical one, thus giving rise to an increase of the time required for the NF data acquisition. In this section, the unified theory of spiral scannings for nonspherical antennas is applied to the spherical spiral scanning. Two effective NF–FF transformations with spherical spiral scanning for nonspherical antennas have been proposed in [30]. The former, suitable for elongated antennas, uses a prolate ellipsoidal AUT modelling, whereas the latter, tailored for quasi-planar antennas, considers the AUT as enclosed in an oblate ellipsoid. For sake of brevity, only the NF–FF transformation using the prolate ellipsoidal modelling will be explicitly considered. It must be stressed that the described approach makes use of a probe compensated NF–FF transformation, unlike the approach in [30] wherein an ideal probe was assumed.

When considering the AUT as enclosed in the smallest prolate ellipsoid having major and minor semi-axes equal to a and b (see Fig. 24), the bandwidth W_η, the phase factor ψ and the parameterization η relevant to a meridian are again given by (20)–(22).

The results of Section 3 can be then applied to determine the scanning spiral, the optimal parameter for describing it, and the corresponding phase factor. In particular, the spiral is obtained by projecting that wrapping the prolate ellipsoid on the spherical surface via the hyperbolas at $\eta = \text{const}$. By taking into account that $r[\theta(\eta)] = d$ and $\phi_i = 0$ for a spherical spiral, the parametric Equations (17) become:

$$\begin{cases} x = d\sin\theta(\eta)\cos\phi \\ y = d\sin\theta(\eta)\sin\phi \\ z = d\cos\theta(\eta) \end{cases} \tag{43}$$

In the following, some numerical tests assessing the effectiveness of the technique are reported. They refer to a spiral wrapping a sphere having radius $d = 40\lambda$ and to a uniform planar array of elementary

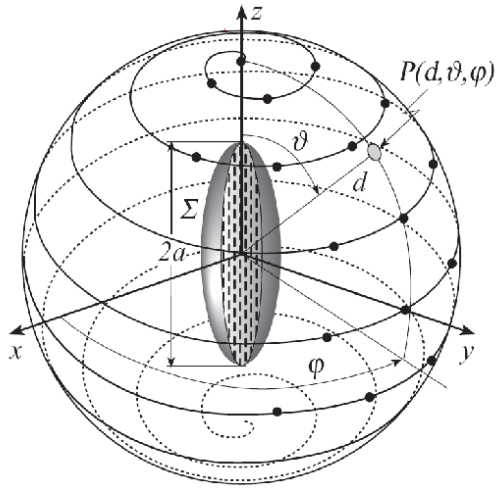

Figure 24. Spherical spiral scan: prolate ellipsoidal AUT modelling.

Huygens sources polarized along the z axis, spaced by 0.5λ. These sources cover an elliptical zone in the plane $y = 0$, with major and minor semi-axes equal to 30λ and 6λ, so that the antenna can be very well fitted by a prolate ellipsoid.

Figure 25 shows a representative reconstruction example of the rotated probe voltage V' on the meridian at $\varphi = 90°$. The accuracy is also confirmed by the values of the maximum and mean–square reconstruction errors (normalized to the voltage maximum value over the sphere) reported in Fig. 26, for $p = q$ ranging from 3 to 10, $\chi = \chi' = 1.20$. As can be seen, the errors decrease up to very low values on increasing the number of retained samples, thus assessing the effectiveness of the representation.

It is worthy to note that an excess bandwidth factor such that the sample spacing is reduced exactly by a factor 11 has been adopted in the zones of the spiral determined by the 120 samples around the poles in order to avoid the growth of the bandlimitation error.

The stability of the developed algorithm has been also investigated by adding random errors to the exact samples. These errors simulate a background noise (bounded to Δa in amplitude and with arbitrary phase) and uncertainties on the voltage samples of $\pm\Delta a_r$ in amplitude and $\pm\Delta\sigma$ in phase. As can be seen (Fig. 27), the algorithm is robust.

The above representation has been applied to accurately recover the NF data needed by the probe compensated NF–FF transformation with spherical scanning [31], modified as described in [12, 18]. Fig. 28

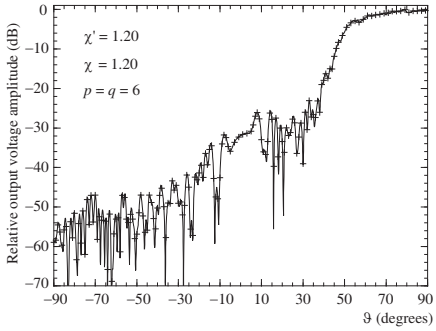

Figure 25. Amplitude of V' on the meridian at $\varphi = 90°$. Solid line: exact. Crosses: interpolated.

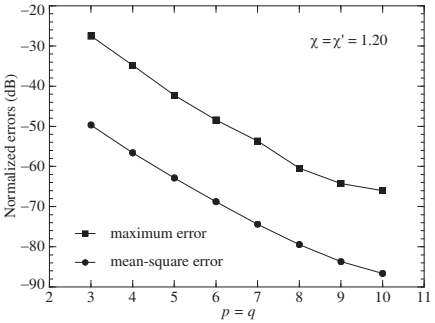

Figure 26. Normalized maximum and mean-square reconstruction errors of V'.

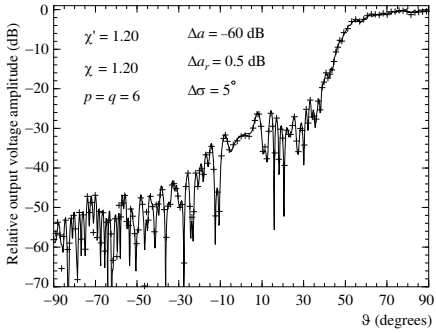

Figure 27. Amplitude of V' on the meridian at $\varphi = 90°$. Solid line: exact. Crosses: interpolated from error affected NF data.

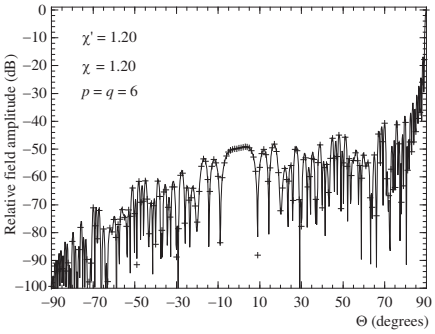

Figure 28. E-plane pattern. Solid line: exact. Crosses: reconstructed from NF data acquired via the spherical spiral scanning.

shows the reconstruction of the E-plane antenna pattern. As can be seen, the exact and recovered fields are indistinguishable, thus assessing the effectiveness of the approach. Note that the number of samples on the spiral is 17 974, significantly less than that (95 504) required by the approach proposed in [19]. In particular, the number of "regular samples" at spacing $\Delta\xi$ is 15 574, whereas the number of "extra samples" at reduced spacing is 2 400. Moreover, the number of used samples results to be much less than that (130 562) needed by the NF–FF transformation [31].

8. CONCLUSION

An efficient sampling representation to reconstruct the EM field radiated by non-spherical antennas on a rotational surface from a nonredundant number of its samples on a spiral wrapping the surface has been developed. The results are general, since they are valid for any spiral lying on surfaces obtained by rotating a meridian curve external to the cone of vertex at the observation point and tangent to the rotational surface modelling the AUT. This new unified theory has been applied to spirals wrapping the conventional scanning surfaces employed in the NF–FF transformations. Numerical tests have confirmed the effectiveness of the approach in reducing the truncation error and the number of data. Although, the optimal spirals, the corresponding phase factors and parameterizations have been heuristically determined, the NF–FF transformations based on this theory work very well as assessed by the numerical tests and some preliminary experimental results.

REFERENCES

1. Yaghjian, A. D., "An overview of near-field antenna measurements," *IEEE Trans. Antennas Propagat.*, Vol. 34, 30–45, January 1986.
2. "Special issue on near-field scanning techniques," *IEEE Trans. Antennas Propagat.*, Vol. 36, 727–901, June 1988.
3. Gennarelli, C., G. Riccio, F. D'Agostino, and F. Ferrara, *Near-Field–Far-Field Transformation Techniques*, Vol. 1, CUES, Salerno, Italy, 2004.
4. Bucci, O. M. and G. Franceschetti, "On the spatial bandwidth of scattered fields," *IEEE Trans. Antennas Propagat.*, Vol. 35, 1445–1455, December 1987.
5. Bucci, O. M., C. Gennarelli, and C. Savarese, "Representation of electromagnetic fields over arbitrary surfaces by a finite and nonredundant number of samples," *IEEE Trans. Antennas Propagat.*, Vol. 46, 351–359, March 1998.
6. Gennarelli, C., G. Riccio, V. Speranza, and C. Savarese, "Fast and accurate interpolation of radiated fields over a cylinder," *Progress In Electromagnetics Research*, PIER 8, 349–375, 1994.
7. Ferrara, F., C. Gennarelli, R. Guerriero, G. Riccio, and C. Savarese, "An efficient near-field to far-field transformation using the planar wide-mesh scanning," *Journal of Electromagnetic Waves and Applications*, Vol. 21, No. 3, 341–357, 2007.

8. Bucci, O. M., C. Gennarelli, G. Riccio, and C. Savarese, "Near-field–far-field transformation from nonredundant plane-polar data: Effective modellings of the source," *IEE Proc. — Microw., Antennas Propagat.*, Vol. 145, 33–38, 1998.
9. Bucci, O. M., F. D'Agostino, C. Gennarelli, G. Riccio, and C. Savarese, "NF–FF transformation with plane-polar scanning: Ellipsoidal modelling of the antenna," *Automatika*, Vol. 41, 159–164, 2000.
10. Bucci, O. M., C. Gennarelli, G. Riccio, and C. Savarese, "NF–FF transformation with cylindrical scanning: An effective technique for elongated antennas," *IEE Proc. — Microw., Antennas Propagat.*, Vol. 145, 369–374, October 1998.
11. D'Agostino, F., F. Ferrara, C. Gennarelli, G. Riccio, and C. Savarese, "NF–FF transformation with cylindrical scanning from a minimum number of data," *Microw. Opt. Technol. Lett.*, Vol. 35, 264–270, November 2002.
12. Bucci, O. M., F. D'Agostino, C. Gennarelli, G. Riccio, and C. Savarese, "Data reduction in the NF–FF transformation technique with spherical scanning," *Journal of Electromagnetic Waves and Applications*, Vol. 15, 755–775, 2001.
13. Bolomey, J. C., et al., "Rapid near-field antenna testing via array of modulated scattering probes," *IEEE Trans. Antennas Propagat.*, Vol. 36, 804–814, June 1988.
14. Yaccarino, R. G., L. I. Williams, and Y. Rahmat-Samii, "Linear spiral sampling for the bipolar planar antenna measurement technique," *IEEE Trans. Antennas Propagat.,* Vol. 44, 1049–1051, July 1996.
15. Bucci, O. M., C. Gennarelli, G. Riccio, and C. Savarese, "Nonredundant NF–FF transformation with helicoidal scanning," *Journal of Electromagnetic Waves and Applications*, Vol. 15, 1507–1519, 2001.
16. Bucci, O. M., F. D'Agostino, C. Gennarelli, G. Riccio, and C. Savarese, "Probe compensated FF reconstruction by NF planar spiral scanning," *IEE Proc. — Microw., Antennas Propagat.*, Vol. 149, 119–123, April 2002.
17. Bucci, O. M., F. D'Agostino, C. Gennarelli, G. Riccio, and C. Savarese, "NF–FF transformation with spherical spiral scanning," *IEEE Antennas Wireless Propagat. Lett.*, Vol. 2, 263–266, 2003.
18. D'Agostino, F., F. Ferrara, C. Gennarelli, G. Riccio, and C. Savarese, "Directivity computation by spherical spiral scanning in NF region," *Journal of Electromagnetic Waves and*

Applications, Vol. 19, 1343–1358, 2005.

19. D'Agostinov, F., C. Gennarelli, G. Riccio, and C. Savarese, "Theoretical foundations of near-field–far-field transformations with spiral scannings," *Progress In Electromagnetics Research*, PIER 61, 193–214, 2006.
20. Costanzo, S. and G. Di Massa, "Near-field to far-field transformation with planar spiral scanning," *Progress In Electromagnetics Research*, PIER 73, 49–59, 2007.
21. Costanzo, S. and G. Di Massa, "Far-field reconstruction from phaseless near-field data on a cylindrical helix," *Journal of Electromagnetic Waves and Applications*, Vol. 18, No. 8, 1057–1071, 2004.
22. Bucci, O. M., G. D'Elia, and M. D. Migliore, "Advanced field interpolation from plane-polar samples: Experimental verification," *IEEE Trans. Antennas Propagat.*, Vol. 46, 204–210, February 1998.
23. Ricciardi, G. F. and W. L. Stutzman, "A near-field to far-field transformation for spheroidal geometry utilizing an eigenfunction expansion," *IEEE Trans. Antennas Propagat.*, Vol. 52, 3337–3349, December 2004.
24. D'Agostino, F., F. Ferrara, C. Gennarelli, R. Guerriero, and M. Migliozzi, "An effective NF-FF transformation technique with planar spiral scanning tailored for quasi-planar antennas," *IEEE Trans. Antennas Propagat.*, Vol. 56, 2981–2987, September 2008.
25. Paris, D. T., W. M. Leach, Jr., and E. B. Joy, "Basic theory of probe-compensated near-field measurements," *IEEE Trans. Antennas Propagat.*, Vol. 26, 373–379, May 1978.
26. D'Agostino, F., F. Ferrara, C. Gennarelli, R. Guerriero, and M. Migliozzi, "Near-field–far-field transformation technique with helicoidal scanning for elongated antennas," *Progress In Electromagnetics Research B*, Vol. 4, 249–261, 2008.
27. D'Agostino, F., F. Ferrara, C. Gennarelli, R. Guerriero, M. Migliozzi, and G. Riccio, "NF–FF Transformation with helicoidal scanning: An effective source modelling for elongated antennas," *Int. Jour. of Microw. Opt. Technol.*, Vol. 3, 275–282, July 2008.
28. Leach, W. M., Jr. and D. T. Paris, "Probe compensated NF measurements on a cylinder," *IEEE Trans. Antennas Propagat.*, Vol. 21, 435–445, July 1973.
29. D'Agostino, F., F. Ferrara, C. Gennarelli, R. Guerriero, J. A. Fordham, M. Migliozzi, and C. Rizzo, "Experimental

validation of the NF–FF transformation with helicoidal scanning suitable for elongated antennas," *Proc. of AMTA 2008*, 304–308, Boston, USA, November 2008.

30. D'Agostino, F., F. Ferrara, C. Gennarelli, R. Guerriero, M. Migliozzi, and G. Riccio, "A nonredundant near-field to far-field transformation with spherical spiral scanning for nonspherical antennas," *The Open Electrical & Electronic Eng. Jour.*, Vol. 3, 4–11, 2009.
31. Hansen, J. E. (ed.), *Spherical Near-Field Antenna Measurements*, IEE Electromagnetic Waves Series, Peter Peregrinus, London, UK, 1998.